Available online at www.sciencedirect.com
SCIENCE DIRECT®
Journal of Sound and Vibration 270 (2004) 559–572
JOURNAL OF SOUND AND VIBRATION
www.elsevier.com/locate/jsvi

Computational aeroacoustic simulations of leading-edge slat flow

K. Takeda[a,*], X. Zhang[a], P.A. Nelson[b]

[a] School of Engineering Sciences, University of Southampton, Southampton SO17 1BJ, UK
[b] Institute of Sound and Vibration, University of Southampton, Southampton SO17 1BJ, UK

Accepted 15 September 2003

Abstract

High-lift devices on modern airliners are a major contributor to overall airframe noise. In this paper the aeroacoustics of leading-edge slat devices in a high-lift configuration are investigated computationally. A hierarchical methodology is used to enable the rapid evaluation of different slat configurations. The overall goal is to gain a deeper understanding of the noise generation and amplification mechanisms in and around the slat, and the effects of slat system geometry.

In order to perform parametric studies of the aeroacoustics, a simplified 2-D model of the slat is used. The flow and aeroacoustics are computed using a compressible, unsteady, Reynolds-Averaged Navier-Stokes code. A robust buffer zone boundary condition is used to prevent the reflection of outgoing acoustic waves from contaminating the long-time solution. A Ffowcs Williams–Hawkings solver is used to compute the far field acoustic field from the unsteady flow solution and determine the directivity. The spanwise correlation length used is derived from experimental data of this high-lift configuration. The effect of spanwise correlation length on the acoustic far field is examined.

The aeroacoustics of the slat system are largely governed by the geometry, especially in terms of slat overlap. We perform a study of the effects of trailing edge thickness, horizontal and vertical overlap settings for the slat on near field wave propagation and far field directivity. The implications for low-noise leading edge slat design are discussed.

1. Introduction

Airframe noise is a significant contributor to the overall noise signature of modern commercial airliners [1]. The most significant contributors to airframe noise are landing gear and high-lift

*Corresponding author. Tel.: +44-23-8059-4467; fax: +44-23-8059-3058.
E-mail address: ktakeda@soton.ac.uk (K. Takeda).

0022-460X/$ - see front matter © 2003 Elsevier Ltd. All rights reserved.
doi:10.1016/j.jsv.2003.09.046

devices [2]. In the latter case, the unsteady flow in and around leading-edge slats and trailing edge flap systems is known to be responsible for significant noise generation. In particular, slat noise has been shown to be a dominant noise source [3,4] and is exacerbated by the fact that slats are typically installed as full-span devices.

While the character of radiated noise from the airframe is generally broadband in nature, strong tones have been observed to occur in both experiments and full-scale flyover tests. The presence of these tones is highly undesirable due to their effect in significantly increasing the perceived noise level. The origin of many of these tones has been found to be the region around the leading edge slat and trailing edge flap [3–5]. Tam and Pastouchenko [6] studied the generation of these gap tones using a wall jet model for the slat or flap gap exit. Here this wall jet model is extended to include the slat cove and main element leading edge in order to examine the effects of overlap and gap settings, as well as a blunt trailing edge to examine the effect of trailing edge thickness.

Section 2 describes the simplified slat model used to characterize the radiated tonal noise in terms of geometric parameters such as trailing edge thickness, slat overlap and gap settings. Section 3 describes the unsteady Reynolds-Averaged Navier-Stokes approach used to model the near field and the Ffowcs Williams–Hawkings (FW–H) solver used to compute the far field directivity. Results are presented in Section 4 with details of the geometric effects on the radiated sound field. A discussion of the results is included in Section 5 as is followed by concluding remarks in Section 6.

2. Idealized slat model

The aeroacoustics of a given slat configuration, such as that shown in Fig. 1(a), is highly dependent upon the local geometry and so isolating the underlying noise mechanisms is not straightforward. In an attempt to isolate the geometric effects on the radiated noise field a simplified 2-D model with an idealized geometry is used in this study. The spanwise extent of the slat system is assumed to be sufficiently large that 3-D effects can be neglected. The effect of two-dimensionality on computing the radiated noise levels is taken into consideration in the Acoustic Analogy solver and is discussed in Section 4. The aim here is not to exactly replicate the experimental data of a full-flight configuration wind tunnel model, but to use an idealized model

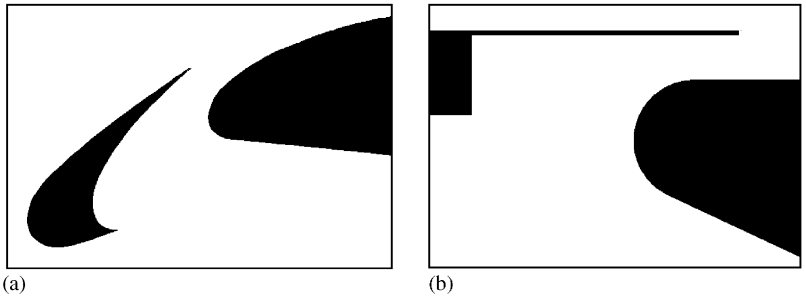

Fig. 1. (a) Typical slat geometry, (b) idealized slat geometry.

that includes the major flow physics pertaining to the slat noise problem. Tam and Pastouchenko [6] used a wall jet model to uncover a resonance mechanism for acoustic feedback in gap flows and developed a model for the tone frequency as a function of gap height, local flow speed and the local speed of sound. In this paper the wall jet model of Tam and Pastouchenko is extended to include the slat cove region and main element leading edge. Experimental measurements of a three-element high-lift wing system [7,8] show the behaviour of the slat cove flow to closely resemble that over a backward-facing step. Fig. 1(b) shows the simplified model, with the cove modelled as a backward-facing step and the main element leading edge angled to represent the wing system at a given flight angle of attack. This simplified slat system model enables a systematic study of slat overlap and gap to be carried out. An aerodynamically *blunt* slat trailing edge is included so that the effect of trailing edge thickness may be examined. The dimensions of the computational model are based on a $\frac{1}{5}$th scale L1T2 2-D National High Lift model used during experimental testing [7,8], which has a reference main wing chord of 0.764 m. The computational grid is non-dimensionalized by the slat cove height, which is 2.75% of the reference main wing chord. The size of the recirculation region and flow Mach number through the slat gap are in reasonable agreement with experimental results [7,8], given the differences in geometry. The trailing edge shedding frequency for the thin trailing edge case is in good agreement with those estimated using Particle Image Velocimetry [8]. Hence the essential flow physics pertinent to the slat problem appear to be captured in the idealized model.

3. Computational method

In order to compute the near field flow a compressible finite-volume unsteady Reynolds-Averaged Navier-Stokes solver (URANS) is used. For this work the code is used in 2-D mode to solve the compressible time-dependent thin-layer Navier-Stokes equations in conservative form on a curvilinear multi-block structured grid. The code uses an implicit solver in time with approximate factorization and 10 sub-iterations per physical timestep, and is second order accurate in space through the use of biased upwind differencing. In order to account for the effects of Reynolds stresses on the short-time averaged flow quantities the two-equation Wilcox k–ω turbulence model is used [9] integrated to the wall using grids that have a y^+ of $O(1)$. An adiabatic no-slip boundary condition is used along solid walls.

To prevent the reflection of spurious waves from the edge of the computational domain, absorbing boundary conditions are used. Explicit buffer zone blocks are placed around the computational domain and an exponential damping function $\sigma(x)$ is applied (1) to damp the conserved variables to a target solution (2):

$$\sigma(x) = \varepsilon\left(\frac{L-x}{L}\right)^{\beta}, \tag{1}$$

where L is the buffer zone width, x the grid co-ordinate, ε the damping coefficient and β a shape parameter;

$$\bar{Q}_{new}^{(n+1)} = \bar{Q}_{old} - \sigma(x)(\bar{Q}_{old}^{(n+1)} - \bar{Q}_{target}). \tag{2}$$

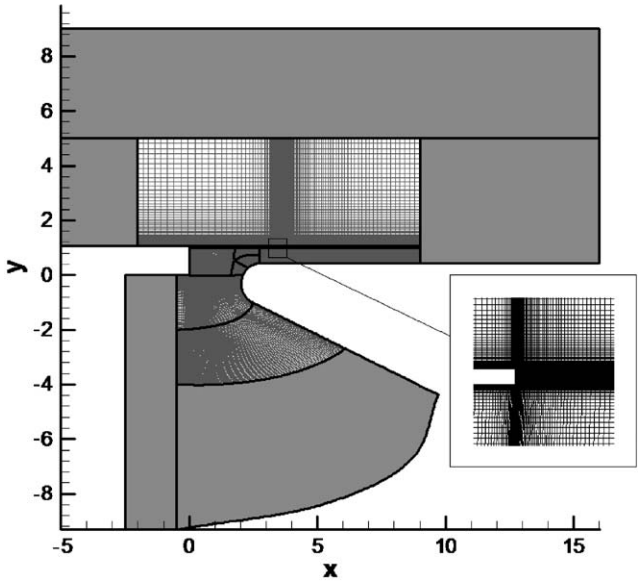

Fig. 2. 14-block computational grid, buffer zone blocks shaded. Slat trailing edge grid detail also shown.

This buffer zone formulation can effectively prevent the reflection of spurious waves, although the exact specification of damping coefficient and shape parameter may have to be changed between test cases to obtain optimum results. Fig. 2 shows a typical computational grid with buffer zone blocks shaded. Fig. 3 illustrates the effectiveness of the buffer zone boundary condition for a typical test case presented here (acoustic pressure contours shown). For the results presented here grids with 13 and 14 blocks are used, with over 75 000 gridpoints/case. Five buffer zone blocks are used, which account for approximately 20% of the total number of gridpoints.

The far field acoustics are computed using the FW–H equation, based on the Farassat 1A formulation [10], and has been previously validated using a variety of cavity test cases [11,12]. The FW–H equation in differential form may be written as

$$\Box^2(\mathrm{H}p'(x,t)) = \frac{\partial^2}{\partial x_i \partial x_j}(T_{ij}\mathrm{H}) - \frac{\partial^2}{\partial x_i}\left(L_{ij}\frac{\partial \mathrm{H}}{\partial x_j}\right) + \frac{\partial}{\partial t}\left(\rho_0 U_i \frac{\partial \mathrm{H}}{\partial x_j}\right), \tag{3}$$

where $\Box^2 = (1/c_0^2)\partial^2/\partial t^2 - \partial^2/\partial x_i^2$ is the wave operator, c_0 is the ambient speed of sound, t is the observer time, p' is the acoustic pressure, ρ_0 the ambient density and $\mathrm{H} = \mathrm{H}(f)$ is the Heaviside function for an integration surface $f = 0$. The first term on the right-hand side of the equation represents the volume source (quadrupole) term. The second term represents the unsteady body force source (dipole) term and the third (monopole) term represents sound generation due to volume displacement of the surface. The terms U_i and L_{ij} are defined as

$$U_i = \left(1 - \frac{\rho}{\rho_0}\right)v_i + \frac{\rho u_i}{\rho_0}, \tag{4}$$

$$L_{ij} = P'_{ij} + \rho u_i(u_j - v_j). \tag{5}$$

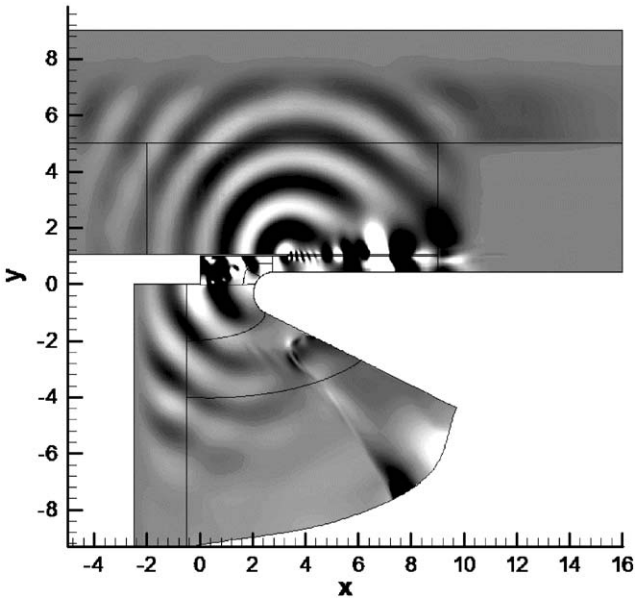

Fig. 3. Buffer zone performance for typical baseline test case. Acoustic pressure contours shown (± 5 Pa).

Using a standard Green's function approach it is possible to write Eq. (3) in the following integral form:

$$4\pi \mathrm{H} p'(x,t) = \frac{\partial^2}{\partial x_i \partial x_j} \int_V \left[\frac{T_{ij}}{r|1-M_r|}\right]_{ret} \mathrm{d}V - \frac{\partial}{\partial x_i} \int_S \left[\frac{L_{ij}\hat{n}_j}{r|1-M_r|}\right]_{ret} \mathrm{d}S + \frac{\partial}{\partial t} \int_S \left[\frac{U_i \hat{n}_i}{r|1-M_r|}\right]_{ret} \mathrm{d}S. \tag{6}$$

Eq. (6) requires derivatives to be taken at the observer time and location, which makes it troublesome to compute. In order to simplify the computation the approach described by Farassat [10] to manipulate Eq. (6) into a form relative to the source time and location is followed. This form is known as the integral solution 1A,

$$p'(\mathbf{x},t) = p'_T(\mathbf{x},t) + p'_L(\mathbf{x},t) + p'_Q(\mathbf{x},t), \tag{7}$$

where

$$4\pi p'_T = \int_S \left[\frac{\rho_0(\dot{U}_n + U_{\dot{n}})}{r(1-M_r)^2}\right]_{ret} \mathrm{d}S + \int_S \left[\frac{\rho_0 U_n (r\dot{M}_r + c_0 M_r - c_0 M^2)}{r^2(1-M_r)^3}\right]_{ret} \mathrm{d}S, \tag{8}$$

$$4\pi p'_L = +\frac{1}{c_0}\int_S \left[\frac{\dot{L}_r}{r(1-M_r)^2}\right]_{ret} \mathrm{d}S + \int_S \left[\frac{L_r - L_M}{r^2(1-M_r)^2}\right]_{ret} \mathrm{d}S + \frac{1}{c_0}\int_S \left[\frac{L_r(r\dot{M}_n + c_0 M_r - c_0 M^2)}{r^2(1-M_r)^3}\right]_{ret} \mathrm{d}S \tag{9}$$

and $p'_Q = (\mathbf{x}, t)$, which accounts for quadrupole sources outside the integration surface, is neglected in this case. In Eqs. (8) and (9) a dot indicates a time derivative and subscript r indicates

a vector projection in the radiation direction. The *ret* subscript indicates integration at retarded source (i.e., emission) time: $\tau = t - |\mathbf{x} - \mathbf{y}|/c_0$, where $\mathbf{y}$ is the source location, and $\mathbf{x}$ is the observer position at time t.

4. Results and analysis

Simulations were carried out for a variety of conditions in order to characterize the near and far acoustic fields with respect to local geometry. The following test cases are presented: baseline test case, thin trailing edge, small slat gap and zero overlap; details of which are given in Table 1. The results presented here are at a Mach number of 0.088 and a Reynolds number of 1 560 015 based on main element chord with HLDs retracted, in order to match the experimental conditions of the NHL model tests of Takeda et al. [7,8].

Mach number contours and streamtraces for the mean flow of the baseline test case are shown in Fig. 4. Note the stagnation point on the main element leading edge which corresponds well with the stagnation point behaviour found in experiments [7]. The separation bubble formed within the slat cove reattaches on the slat inner surface upstream of the main element leading edge. The flow can be seen to accelerate through the slat gap and reaches approximately twice the freestream Mach number. Visualizations of the unsteady flow clearly show vortex shedding at the slat's blunt trailing edge.

Fig. 5 shows the unsteady pressure time history taken at three points around the trailing edge. The dot–dashed and dotted lines show the pressure at 0.065%c upstream of the trailing edge on the upper and lower surfaces respectively. The principal frequency is 9.1 kHz which corresponds to the trailing edge shedding frequency and a Strouhal number of 0.30 based on trailing edge thickness and freestream velocity. Of note is the 180° phase difference between the pressure at these points, indicative that the trailing edge is acting as a dipole sound source. Fig. 6 is an instantaneous snapshot of the acoustic field for the baseline test case showing sound emanating from the slat trailing edge. Waves propagating through the slat gap diffract around the main element leading edge but do not radiate beyond $\theta > 270°$, where θ is zero along the positive x-axis and increases in the anti-clockwise direction. For the baseline case the acoustic wavelength of the trailing edge source is a fraction of the slat gap and as the wave strikes the main element surface it is reflected back towards the trailing edge, as highlighted in Tam and Pastouchenko [6]. The accelerated flow through the slat gap acts to convect the reflected wave which then interacts with

Table 1
Slat test case geometry relative to main wing mean chord

Test case	Overlap (%)	Gap (%)	Trailing edge thickness (%)
Baseline	+1.5	1.0	0.065
Thin trailing edge	+1.5	1.0	0.033
Small gap	+1.5	0.5	0.065
Zero overlap	0.0	1.0	0.065

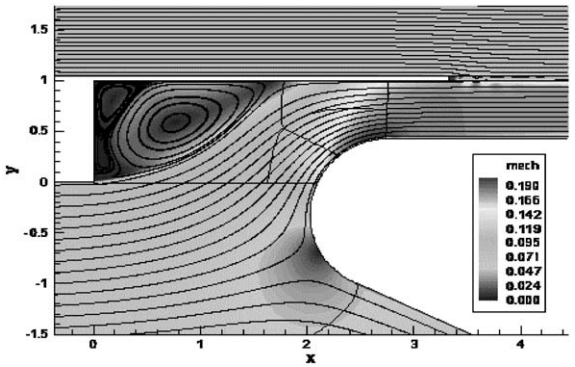

Fig. 4. Mean flowfield for baseline test case. Mach number contours and streamtraces shown.

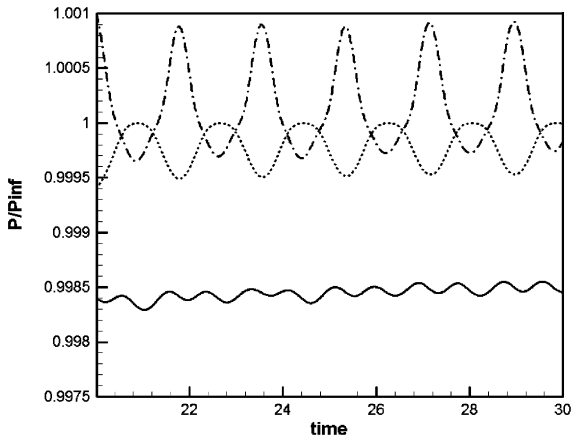

Fig. 5. Unsteady pressure time histories around slat trailing edge. —— trailing edge, — · — upper surface, - - - - - lower surface.

the trailing edge wake. Upstream the propagating wave radiates past the slat cove lip, but is also reflected back downstream after it strikes the upstream slat cove wall.

Fig. 7 shows the acoustic near field for the thin trailing edge case in which the conditions are identical to the baseline case except that the trailing edge thickness is halved to 0.033%c. The vortex shedding frequency is 15 kHz which translates to a Strouhal frequency of 0.25 based on trailing edge thickness and freestream velocity, which agrees well the frequency measured experimentally for the full three-element NHL wing on which the idealized model is based [7,8]. The change in shedding frequency with trailing edge thickness indicates that the resonant feedback mechanism described by Tam and Pastouchenko [6] is not strong enough to cause lock-on in this case where the trailing edge is finite. The acoustic pressure contours are significantly different to those for the baseline case with two distinct lobes above the slat due to the reflection and downstream convection of the waves between the trailing edge and main element suction surface. This can be seen clearly in Fig. 8 which shows a time-history of the acoustic near field around the slat cove and trailing edge for half a shedding cycle. Upstream waves inside the slat gap and cove are seen to fully diffract around the main element trailing edge due to the reduced

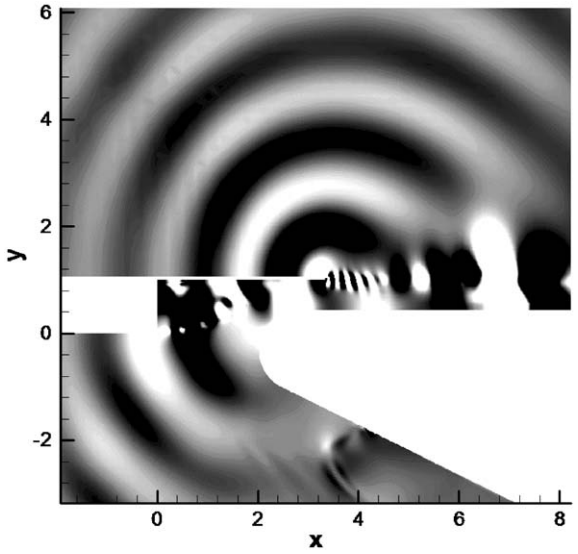

Fig. 6. Acoustic near field for baseline test case. Acoustic pressure contours shown (± 5 Pa).

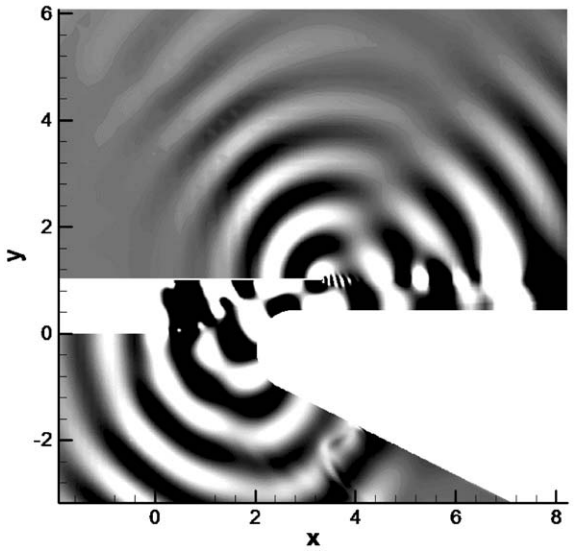

Fig. 7. Acoustic near field for thin trailing edge case. Acoustic pressure contours shown (± 5 Pa).

wavelength compared to the baseline case. Waves propagating directly upstream and reflecting on the slat inner wall appear to form a standing wave pattern within the slat cove bounded by the cove shear layer. The upstream wave diffracting around the main element also interacts with the slat cove shear layer that impinges on the slat inner wall at $x = 1.60$, leading to a distinct double-lobe pattern below the slat lip. The nature of this upstream radiation is complicated by the non-uniform mean flow upstream of the slat gap and the presence of the shear layer.

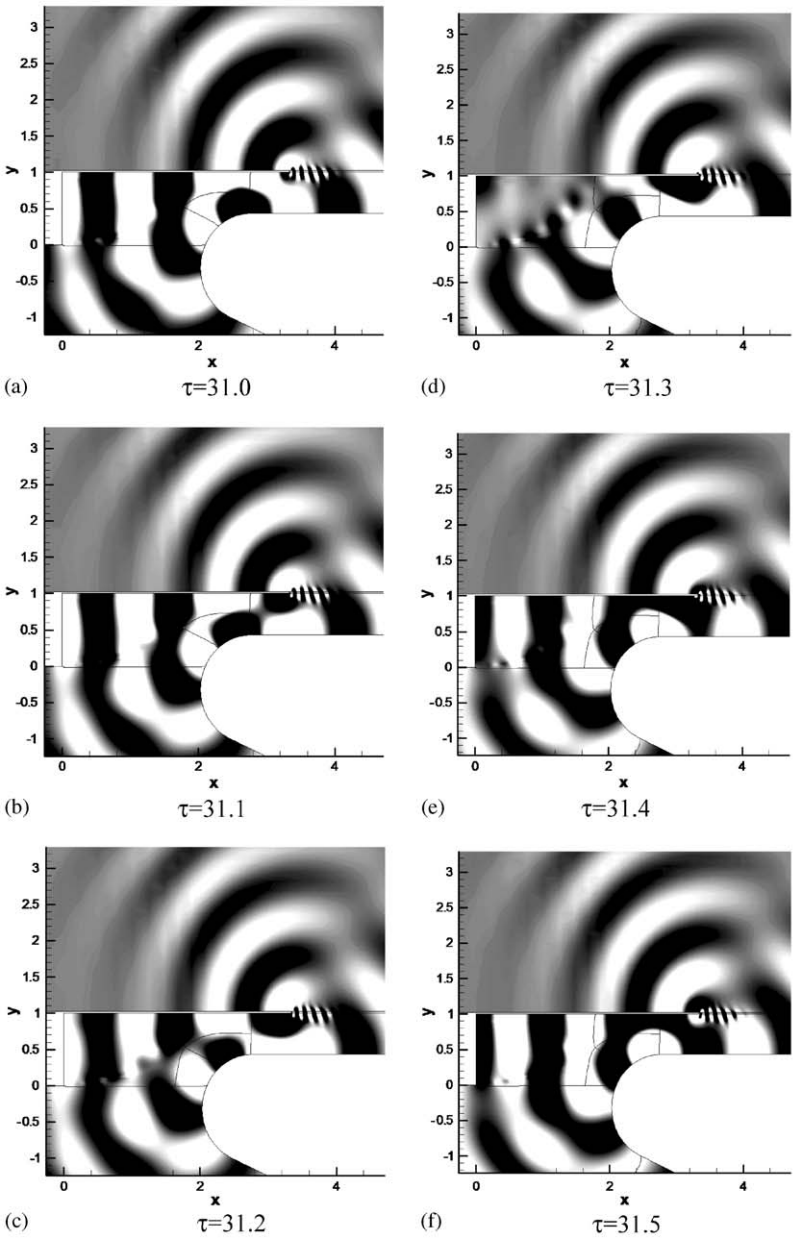

Fig. 8. Time sequence of acoustic near field for thin trailing edge case. Acoustic pressure contours shown (± 5 Pa).

The far field directivity for the baseline and thin trailing edge cases calculated using the FW–H solver are shown in Fig. 9 using an integration surface 0.065%c below the slat for the dominant fundamental frequency. The observers are located on a 10 m radial arc centred about the slat cove lip. In order to compute the far field noise using the FW–H solver from the 2-D near field CFD data it is assumed that the flow is perfectly correlated in the spanwise direction. The spanwise

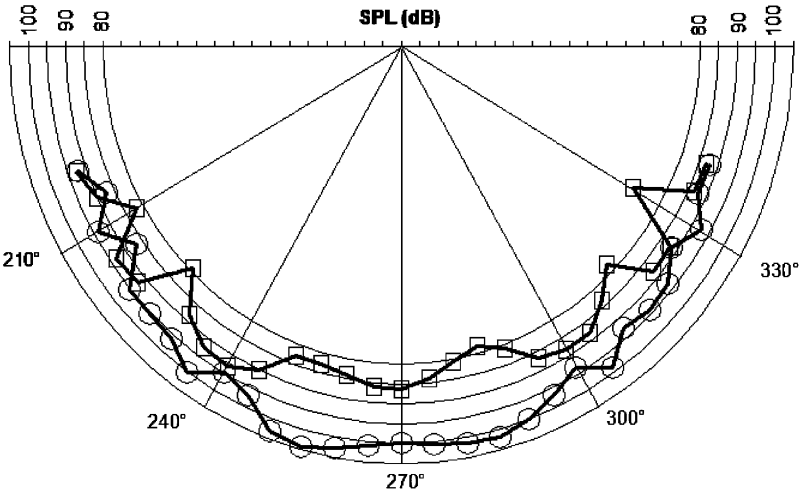

Fig. 9. Far field directivity below slat; squares indicate baseline case, circles indicate thin trailing edge case.

correlation distance used here ($0.15c$) is that measured using two-point streamwise velocity correlation hot-wire anemometry measurements of the $\frac{1}{5}$th scale NHL model (to be published). The far field noise patterns for the baseline and thin trailing edge cases differ significantly both in amplitude and shape. The baseline case radiates efficiently in the upstream arc between 200° and 220°, and in an arc between 230° and 245°. There are distinct lobes directly below the slat and around 300°, although these are 10 dB lower than the upstream lobes. The thin trailing edge case exhibits three upstream lobes around 210°, between 220° and 235° and a strong 104 dB lobe at 255°. The strong lobe at 255° corresponds to the principal radiation direction seen in the near field (Fig. 7) with the origin of the two upstream lobes around 210° and between 220° and 235° also visible in Fig. 8. Downstream there is a weak lobe at 285° and a lobe at 305°, along with a steady decrease in radiated sound pressure level with increasing θ. These lobes appear to originate from the diffraction around the main element leading edge (Fig. 8). Of note is the higher sound level associated with the thin trailing edge case in the far field at $\theta > 220°$ compared with the baseline case.

In order to examine the effect of spanwise correlation distance on far field sound pressure level FW–H computations using different correlation distances were performed for the baseline case with an observer placed 10 m directly above the slat trailing edge, the results of which are shown in Fig. 10. It is clear from this that the spanwise correlation distance is a crucial parameter in determining absolute sound pressure levels. In order to be able to perform quantitatively accurate computations using the acoustic analogy approach, measurements of spanwise correlation distance are necessary whether from experiment or time-accurate 3-D computations.

The mean flowfield for the zero overlap case is shown in Fig. 11. The separation bubble reattaches further downstream on the slat inner wall and has a significantly different structure to the 1.5% overlap cases; the flow in the slat gap is accelerated to a lesser extent than in the baseline case and is deflected upwards behind the trailing edge. A snapshot of the instantaneous acoustic field is shown in Fig. 12, which uses the same contour levels as Figs. 6 and 7. The slat cove shear

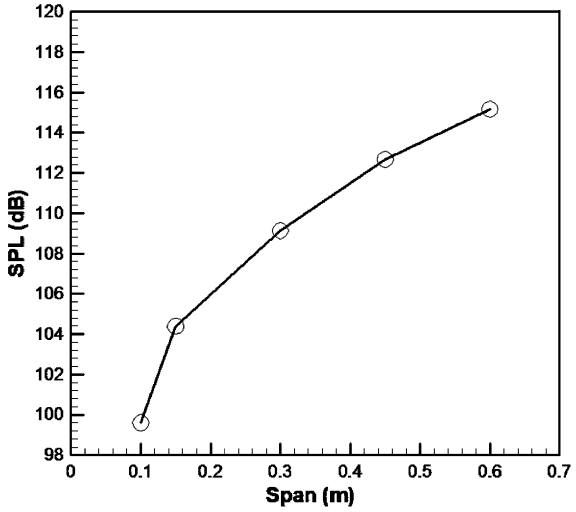

Fig. 10. Far field sound pressure level above slat trailing edge.

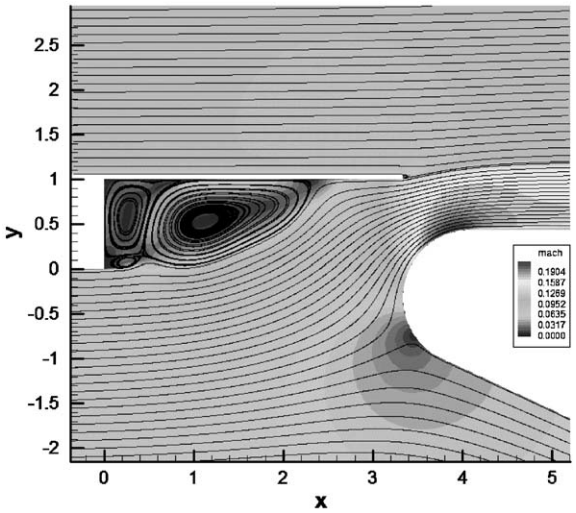

Fig. 11. Mean flowfield for zero overlap test case. Mach number contours and streamtraces shown.

layer and trailing edge shedding are clearly present, although radiation of sound is suppressed. This may be due to the removal of a resonant feedback mechanism similar to that described by Tam and Pastouchenko [6]. Fig. 13 shows the mean flowfield for the small slat gap case. The shear layer from the slat cove lip is forced downwards compared with the baseline case, although the reattachment point remains at the same location. In this case the slat gap is a small fraction of the equivalent wavelength due to trailing edge shedding and examination of the unsteady acoustic pressure (not shown) reveals an absence of radiated sound.

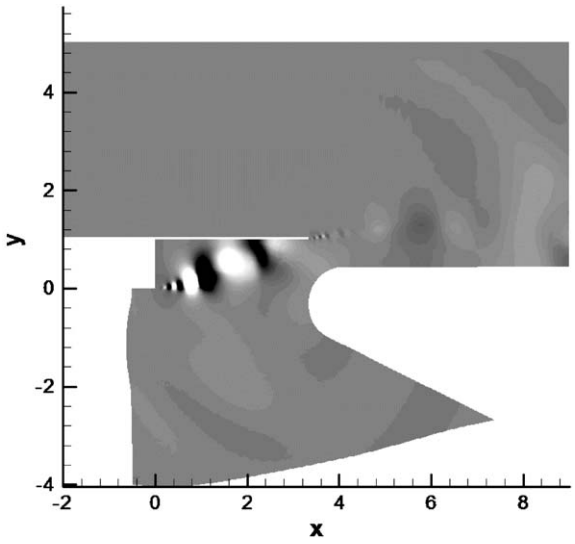

Fig. 12. Acoustic near field for zero overlap case. Acoustic pressure contours shown (± 5 Pa).

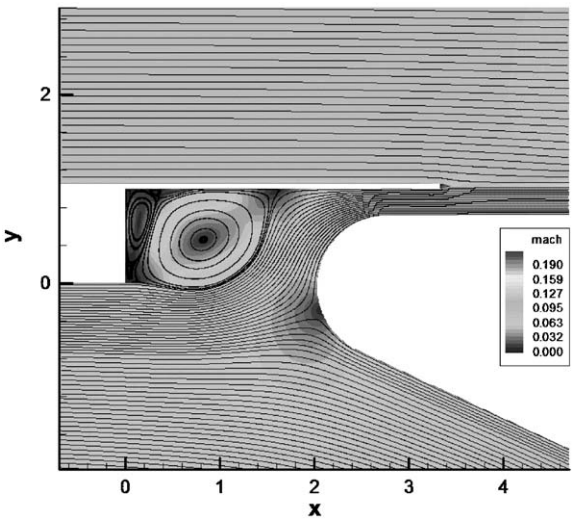

Fig. 13. Mean flowfield for small gap test case. Mach number contours and streamtraces shown.

5. Discussion

The aim of this study has been to develop a model of leading-edge slat flow that allows a systematic study of geometry effects on near and far field acoustics that is computationally amenable and physically representative. The thin trailing-edge case corresponds to the model used by Takeda et al. [7,8] and the mean flow and vortex shedding frequency agree well with those

found in the experiment. The baseline and thin trailing edge cases exhibit significant noise radiation from the slat trailing edge that corresponds to a dipole source radiating at the vortex shedding frequency. Changing the trailing edge thickness causes a change in frequency, although this does not scale as a function of edge thickness exactly, as the Strouhal number is seen to increase with thickness. According to Tam and Pastouchenko's theory [6] acoustic feedback between the trailing edge source and main element surface causes the vortex shedding to lock-on, with the shedding frequency being a function of gap height, local flow velocity and the local speed of sound only. Clearly the shedding frequency is affected by the trailing edge thickness and the acoustic feedback is not strong enough to cause lock-on in this case. Examination of the zero overlap case, in which the possibility of strong acoustic feedback is reduced due to the geometry, shows that there is little sound radiation from the trailing edge even though vortex shedding is still apparent. Similarly with the small slat gap case there is a lack of sound radiation, indicating that although acoustic feedback may not be directly responsible for regulating the frequency of radiated sound, it may be instrumental in determining the cut-on of slat trailing edge tones.

The effect of slat trailing edge shedding frequency on the acoustic far field is significant with the higher frequency exhibiting a more complex upstream lobe structure and greater sound radiation in the downstream arc. The geometry of the slat cove and the presence of the shear layer from the separated flow off the cove lip causes upstream radiation to be dominant. Diffraction of upstream waves from the trailing edge around the main element leading edge seems to be responsible for strong lobes in the downstream direction.

6. Conclusions

A coupled URANS/FW–H approach developed for the study of high-lift device noise has been applied to an idealized slat geometry in order to identify the underlying physical aeroacoustic mechanisms that may be present. The effects of slat geometry on both the near and far field acoustics have been studied and have been shown to be highly dependent on slat/wing geometry. In particular, the presence of an acoustic feedback mechanism seems to be necessary for cut-on of slat tones to occur although it may not be strong enough to regulate vortex shedding in the presence of a finite trailing edge. The frequency of the trailing edge source has been shown to significantly affect the far field acoustics, with diffraction around the main element leading edge being principally responsible for increased downstream radiation at higher frequencies. It is clear that tuning slat/wing geometry is essential to the design low-noise leading-edge slats, and that the application of CAA techniques such as those demonstrated here can help in this endeavour.

References

[1] M.G. Macaraeg, Fundamental investigations of airframe noise, *Fourth AIAA/CEAS Aeroacoustics Conference*, Toulouse, France, AIAA 98-2224, 1998.

[2] D.G. Crighton, Airframe noise, in: *Aeroacoustics of Flight Vehicles: Theory and Practice*, Vol. 1, NASA RP 1258, 1991.

[3] W.R. Stoker, R. Sen, An experimental investigation of airframe noise using a Model-Scale Boeing 777, *39th AIAA Aerospace Sciences Meeting and Exhibit*, Reno, NV, AIAA 2001-0987, January 2001.

[4] B.A. Singer, D.P. Lockard, K.S. Brentner, M.R. Khorrami, M.E. Berkman, M. Choudhari, Computational aeroacoustic analysis of slat trailing-edge flow, *Fifth AIAA/CEAS Aeroacoustics Conference*, Seattle, WA, AIAA 99-1802, May 1999.
[5] M.R. Khorrami, M.E. Berkman, M.M. Choudhari, Unsteady flow computations of a slat with blunt trailing edge, *American Institute of Aeronautics and Astronautics Journal* 38 (11) (2000) 2050–2058.
[6] C.K.W. Tam, N. Pastouchenko, Gap tones: a component of airframe noise, *38th AIAA Aerospace Sciences Meeting and Exhibit*, Reno, NV, AIAA 2000-0606, January 2000.
[7] T. Takeda, G.B. Ashcroft, X. Zhang, Unsteady aerodynamics of slat cove flow in a high-lift device configuration, *39th AIAA Aerospace Sciences Meeting and Exhibit*, Reno, NV, AIAA 2001-0706, January 2001.
[8] K. Takeda, X. Zhang, P.A. Nelson, Unsteady aerodynamics and aeroacoustics of a high-lift device configuration, *40th AIAA Aerospace Sciences Meeting and Exhibit*, Reno, NV, AIAA 2002-0570, January 2002.
[9] D.C. Wilcox, *Turbulence Modeling for CFD*, DCW Industries, La Cañada, CA, 1993.
[10] F. Farrasat, G.P. Succi, The prediction of helicopter discrete frequency noise, *Vertica* 7 (1983) 309–320.
[11] G.B. Ashcroft, K. Takeda, K. Zhang, Computational modelling of the aeroacoustics of a door cavity flow oscillation, *Proceedings of the Seventh International Congress on Sound and Vibration*, Garmisch-Partenkirchen, Germany, July 2000.
[12] G.B. Ashcroft, X. Zhang, A computational investigation of the noise radiated by flow-induced cavity oscillations, *39th AIAA Aerospace Sciences Meeting and Exhibit*, Reno, NV, AIAA 2001-0512, January 2001.